Ultrasonics 93 (2019) 81–92

Contents lists available at ScienceDirect

Ultrasonics

journal homepage: www.elsevier.com/locate/ultras

Modeling and simulation of vibro-thermography including nonlinear contact dynamics of ultrasonic actuator

G. Kolappan Geetha, D. Roy Mahapatra*

Department of Aerospace Engineering, Indian Institute of Science, Bengaluru 560012, India

ARTICLE INFO

Keywords:
Vibro-thermography
Thermo-elasticity
Nonlinear dynamic contact
Harmonics
Ultrasonic horn

ABSTRACT

In this paper, a thermodynamically consistent generalized three-dimensional modeling scheme is developed to simulate vibro-thermography and subsequently perform a quantitative investigation on a test structure. Simulation results are analyzed considering a plate with Structural Features (SF) which are used in a gas turbine engine structural components to reduce structural mass and enhance cooling. The modeling framework includes (i) coupled thermo-elastic heat generation and (ii) effects of various sources of nonlinear vibration arising due to the amplitude of the excitation, the engagement force on the target structure due to the ultrasonic horn, and structural boundary conditions. Transient heat generation behavior in the target structure with SF is analyzed. Dynamic contact models are used to capture the nonlinear harmonics. The effects of engagement force on the dynamic response are analyzed. Simulation results are obtained by incorporating the model in a finite element scheme. The simulation results show that the thermographic inspection can be optimally designed using a relationship between the SF sizes with reference to wavelength based resonance phenomenon. The spectral components obtained at various locations in the SF reveals the presence of both sub- and super-harmonics.

1. Introduction

Vibro-thermography is a hybrid Non-Destructive Testing (NDT) technique, where the structure is excited with a low-frequency actuator and the measurements are obtained using a thermal imager. Among various kinds of exciters used, such as electrodynamic shakers or piezoelectric actuators with different contact or non-contact schemes, piezoelectric transducers with ultrasonic wave energy localization via horn like geometry are the ones widely used for vibro-thermography. A typical ultrasonic horn is designed to amplify its excitation amplitude in the range of 20–30 kHz. It excites elastic waves to propagate in the structure, which further depends on the geometry and material properties of the structure. The waves interact with geometric features and any defects present in the structure. A part of the elastic wave energy gets converted into thermal energy. The distribution of radiative heat flux on the structural surface due to thermal energy transport is imaged with an infrared imaging camera [1–3]. Heat is generated at the location of crack or small geometric features after the start of insonation due to dissipation of mechanical energy near its vicinity [4].

Vibro-thermography is a convenient and reliable NDT technique for inspection of surface or sub-surface features, particularly for inspection of complex structural geometries that are difficult to inspect with other NDT techniques. The inspection time required for this technique is much lower than conventional ultrasonic testing or eddy current inspection, where the inspection probe physically scans the entire specimen. The vibro-thermographic inspection technique is used to detect different kinds of defects in metallic and composite structures. Defects in metallic structure include hidden corrosion [5,6], cracks [7,8], poor adhesion of coating [9], etc. Defects in composite structure include delamination, debonds, impact damage, voids and inclusions [10–12], etc. The gas turbine engine components are provided with pockets to enhance cooling rate and to reduce the mass of the structural component. These pockets can be in the form of cut-out or Structural Feature (SF) of different sizes and shapes. Earlier, Solodov [13,14] used the concept of local defect resonance to enhance defect (delamination) response in nonlinear acoustics and ultrasound thermography. In the present work, a simulation scheme using resonance due to wavelength scale effect of SF is developed, which establishes an optimal relationship between the frequency of excitation and the dimensions of the SF. The developed scheme, enhances the thermographic inspection by maximizing the heat generation in the SF.

Over the last few decades there has been plenty of research in the areas related to vibro-thermography to establish it as a NDT inspection technique [15]. However, the mechanism of heat generation during vibro-thermography is not well reported in the published literature. Earlier works of Farren and Taylor [16] are based on a hardening model

* Corresponding author.
E-mail address: droymahapatra@iisc.ac.in (D. Roy Mahapatra).

https://doi.org/10.1016/j.ultras.2018.11.001
Received 25 March 2018; Received in revised form 13 October 2018; Accepted 4 November 2018
Available online 05 November 2018
0041-624X/

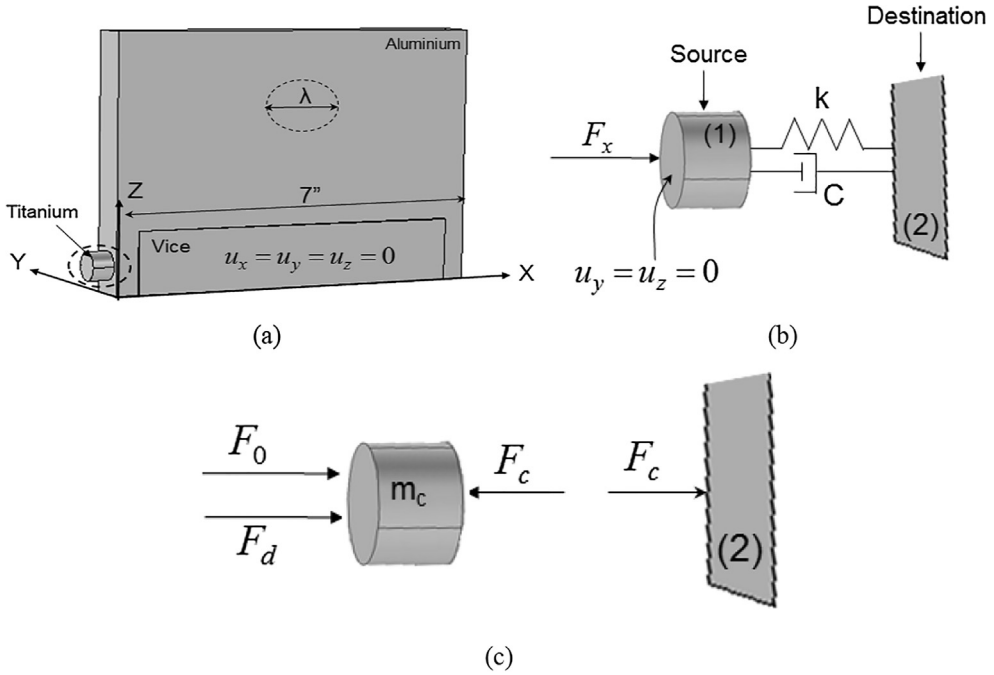

Fig. 1. (a) The horn and the target structure used for the contact mechanics simulation (the dimensions of target structure are given in Fig. 2 (a)). (b) Contact mechanics model using a spring-damper at the contact interface (enlarged view of the circled region in Fig. 1(a)). (c) Free body diagram for the horn and the target structure at the contact interface.

Table 1
Parameter values used in the simulation.

Parameters	Values
Engagement force (F_0)	60 lb
Mass of cylinder (m_c)	0.0078 kg
Mass of horn (m_H)	0.1026 kg
Amplitude of excitation (u_0)	$100/\omega^2$
Frequency of excitation (f_{exc})	30 kHz
Spring constant (k)	1×10^9 N/m
Damping constant (C)	1000 Ns/m
Convective heat transfer coefficient (h)	25 W/(m^{2}K)
Stefan-Boltzmann Constant (σ)	5.670367×10^{-8} (Wm^{-2}K^{-4})

which uses conversion of plastic energy into heat energy. Further, several experiments are performed to measure the conversion rate of plastic work to thermal energy at high strain rate, which enables to quantify the thermal softening in the material [17]. Rosakis [18] proposed a heat transfer mechanism model for thermoplastic heating, which decomposes the strain in the first law of thermodynamics into elastic and plastic parts. Mabrouki [19] developed a numerical model for vibro-thermography based on plastic deformation. The models used in the current state-of-art does not clearly correlate each strain rate component to heat generation in solid. In this paper, the authors have analytically correlated each component of the strain rate with the heat generation in the solid from the fundamental of thermodynamics.

Recently, studies in the areas of vibro-thermography indicate nonlinear vibration phenomena exists in the target structure even when the exciter is sharply tuned to its resonant frequency of excitation [20–23].

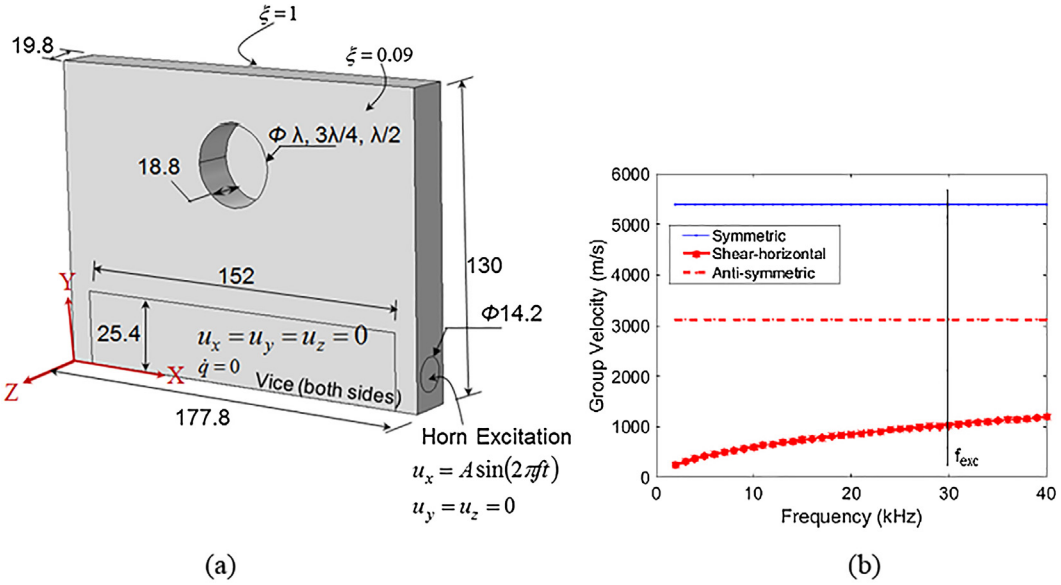

Fig. 2. (a) Schematic shows the dimensions of the target structure, the SF, and various mechanical-thermal boundary conditions used in the simulation. (All units are in mm) (b) Guided wave dispersion curves for the SF with 1 mm thick membrane.

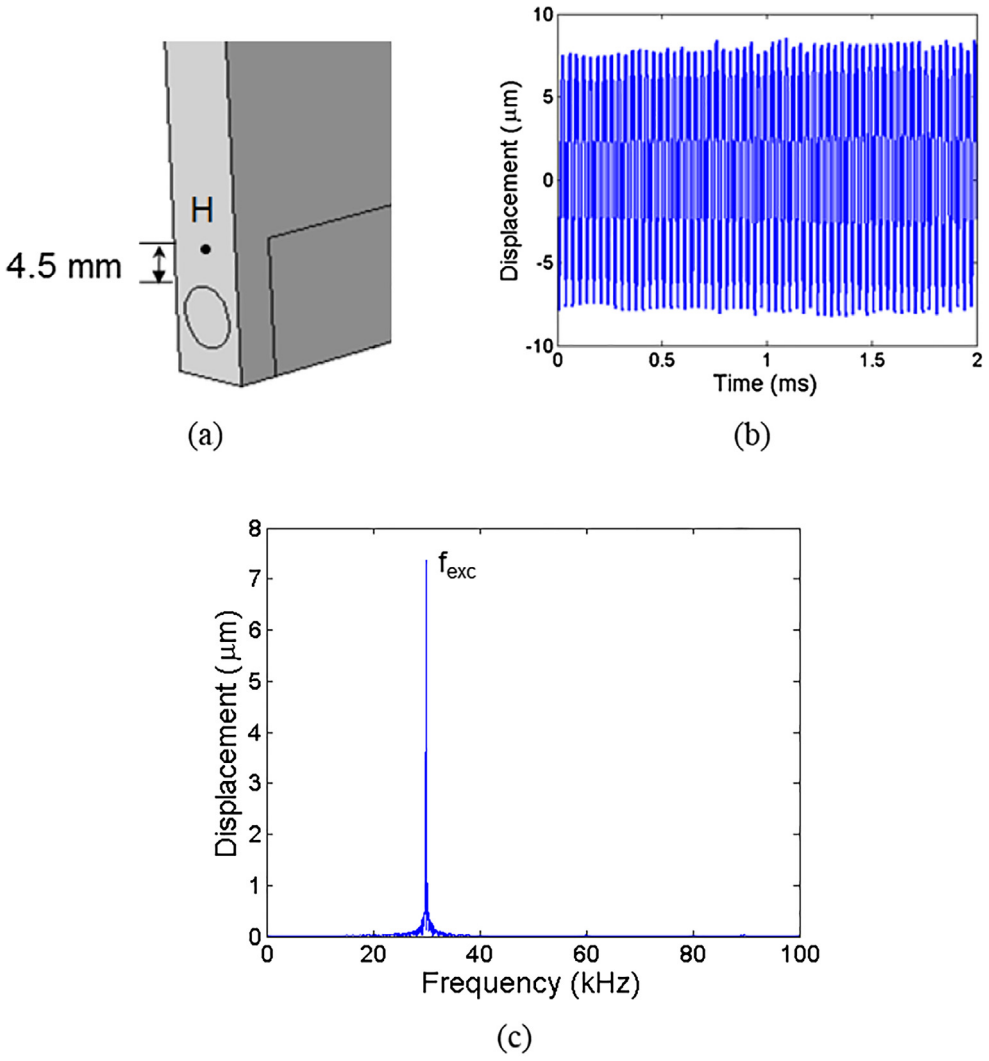

Fig. 3. (a) Schematic depicts the location of point 'H' which is close to the excitation horn. Time-history and frequency spectrum obtained at point 'H' without modeling contact mechanics are shown in (b) and (c) respectively.

The nonlinear vibration phenomenon includes sub-super-harmonics, ultra-sub-harmonics, and chaos. The nonlinear dynamic behavior is hypersensitive to the amplitude of excitation, the engagement force on the target structure due to the ultrasonic horn, and structural boundary conditions. The nonlinear dynamic behavior of the target structure under sonic excitation are discussed in references [21–24] and references therein. Solodov [24] and Feng [21] discusses in detail about experimentally observed nonlinear dynamic phenomenon in the target specimen. The former observed the phenomenon due to self-modulation mode of cracked defects, while the latter observed during the impact interaction between the horn and the target specimen. The later references prove that nonlinearities introduced in the target structure are highly sensitive to excitation mechanism, engagement force and boundary conditions. Han developed a modeling scheme, which generates a chaotic dynamic response [25]. In this scheme, the ultrasonic horn exciter is modeled as lumped mass model where the dimensions varies harmonically with sonic excitation frequency and the target structure is modeled as a rigid mass. Using this model, response is obtained only for the ultrasonic horn driving the target structure. Zheng used a contact-impact mechanism using a lumped mass model to analyze the dynamic behavior between ultrasonic horn and target structure [26]. The lumped models discussed above gives motion in waveforms of the ultrasonic transducer driving the target structure at the contact point. These models essentially capture the dynamic contact interaction between the horn and the target specimen, and ignore the material, geometric effects of the horn and that of the target structure. Therefore, these models cannot be used to estimate the response for every inspection point within the target structure. Further, the results obtained from the models are sensitive to some of the input parameters, such as the initial velocity. However, the general behaviour of the model remains unchanged for wide range of other parameters. In the present paper, a switching nonlinear contact model is used in a finite element simulation scheme to explore the generation mechanisms for nonlinear harmonics in the target structure.

The paper is organized as follows. First, a three-dimensional thermo-elastic coupled model is developed to simulate the phenomenon of heat generation in the target structure (see Section 2.1). In Section 2.2, a nonlinear dynamic contact model is developed to simulate the effects of various sources of nonlinear vibration arising due to the amplitude of excitation, engagement force on the target structure due to the ultrasonic horn, and structural boundary conditions. Section 3 discusses about maximizing the heat generation rate in the SF, using a relationship between the SF sizes with reference to wavelength based resonance phenomenon. Further, the dynamic and the thermal behavior are quantitatively investigated in the test structure having SF. The effects of modeling horn, and introducing contact dynamics between the horn and the target structure is quantitatively investigated in Section 4. The purpose of this work is to incorporate various realistic effects in the

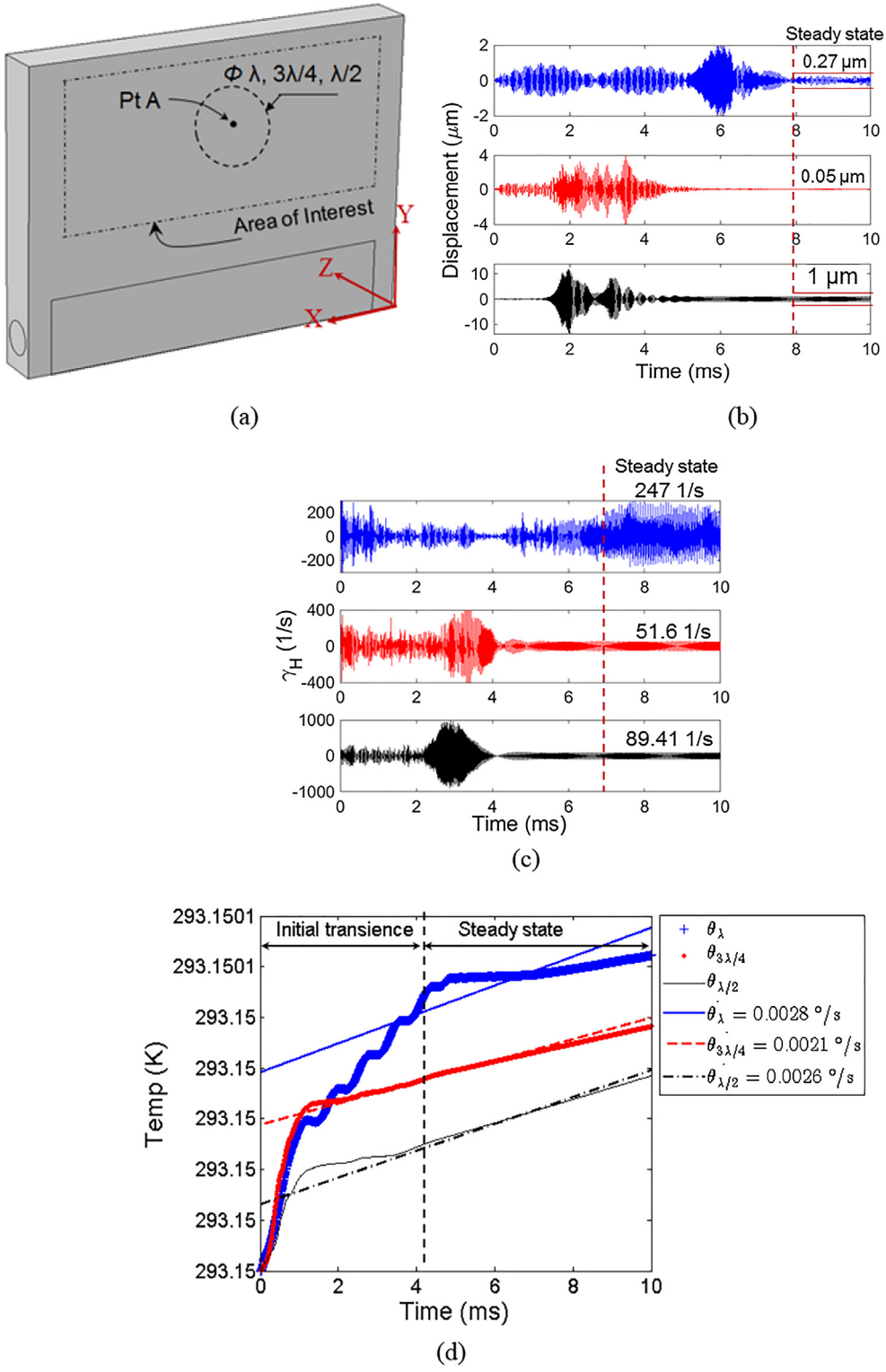

Fig. 4. (a) Schematic depicts location of point A where comparative analysis is done for varying diameters (λ, 3λ/4, λ/2) of SF. For all cases, point 'A' is located at the center of the SF. Displacement-time history, strain rate-time history, and temperature-time history obtained at point A for varying slot sizes are plotted in figures (b), (c) and (d), respectively. In addition, Figure (d) plots temperature rate for various sizes of SF.

vibro-thermography model. The developed model aids in optimizing experimental measurements during vibro-thermography with ultrasonic actuator.

2. Modeling vibro-thermography

To simulate vibro-thermography in a finite element scheme, a thermodynamically consistent generalized three-dimensional modeling scheme is developed in this paper. The modeling framework includes (i) developing a coupled thermo-elastic heat generation scheme, and (ii)

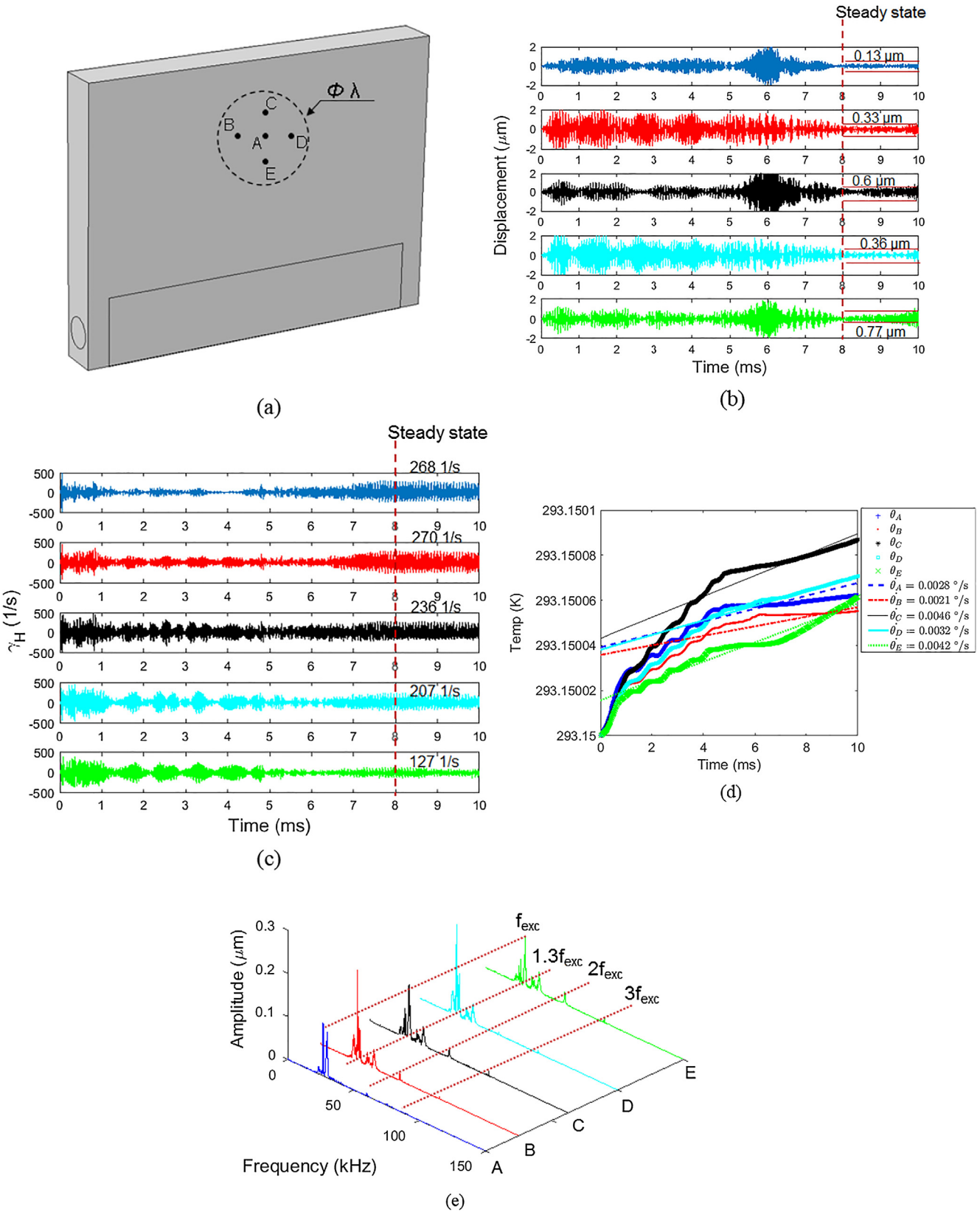

Fig. 5. (a) Schematic illustrates the locations of points 'A', 'B', 'C', 'D' and 'E' on the SF. These points are located on the surface which has emissivity $\xi = 1$. Displacement-time history, strain rate-time (γ_H) history, temperature-time history and frequency spectrum obtained at various points on the SF are plotted in figures (b), (c), (d), and (e), respectively. Figure (d) also plots temperature rate obtained at various points on the SF. These simulation results are obtained without modeling contact mechanics between the horn and the target structure.

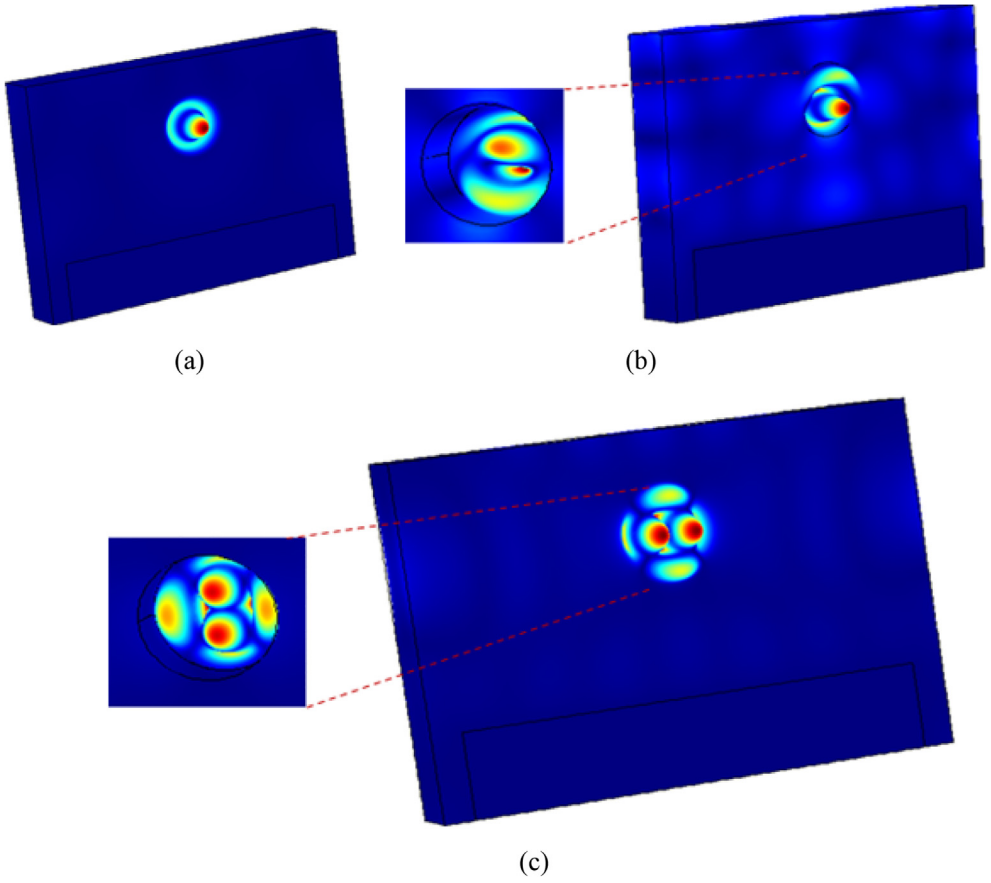

Fig. 6. Resonant mode shapes obtained for various different frequencies. (a) 30.15 kHz, (b) 45.041 kHz, and (c) 61.973 kHz.

developing models for various sources of nonlinear vibration arising from the amplitude of excitation, the engagement force on the target structure due to the ultrasonic horn, and the structural boundary conditions.

2.1. Modeling of heat generation

In last few decades extensive research has been done towards understanding vibro-thermography. To the best of the author's knowledge, existing models do not correlate various components of strain with the heat generation scheme in solids [14,19]. In the present model, a thermodynamically consistent generalized three dimensional coupled thermo-elastic model is formulated from the fundamentals of thermodynamics. The details of mathematical model are discussed below. Following the conventional notations, the overhead dot denotes time derivative, index denotes indicial notation and comma denotes derivatives of field variables with respect to spatial coordinates. The first law of thermodynamics [27] is given by

$$\rho\dot{U} = \dot{\varepsilon}_{ij}\sigma_{ij} + \frac{1}{V}\frac{\delta Q}{dt} = \dot{\varepsilon}_{ij}\sigma_{ij} + r - q_{i,i}, \tag{1}$$

where, U is the specific internal energy, q_i is the heat flux vector, r is the heat supply per unit time and unit volume, σ_{ij} and ε_{ij} are the stress and strain tensor, respectively. The second law of the Clausius-Duhem inequality [27] is given by

$$\rho\dot{s} - \frac{r}{\theta} + \frac{q_{i,i}}{\theta} - \frac{q_i\theta_{,i}}{\theta^2} \geqslant 0, \tag{2}$$

where, s is the specific entropy (state function) and θ is the absolute temperature. Eliminating terms $q_{i,i} - r$ using Eqs. (1) and (2), and further expressing the dissipation inequality in terms of internal energy (U)

$$\gamma \equiv \rho\theta\dot{s} - \rho\dot{U} + \dot{\varepsilon}_{ij}\sigma_{ij} - \frac{q_i\theta_{,i}}{\theta} \geqslant 0. \tag{3}$$

The state functions U and s can be expressed in terms of another state function Helmholtz free energy ψ.

$$\psi = U - s\theta \Rightarrow \dot{U} = \dot{\psi} + \dot{s}\theta + s\dot{\theta}. \tag{4}$$

Substituting equation (4) in (3) gives dissipation inequality in terms of free energy ψ

$$\gamma \equiv -\rho(\dot{\psi} + s\dot{\theta}) + \dot{\varepsilon}_{ij}\sigma_{ij} - \frac{q_i\theta_{,i}}{\theta} \geqslant 0. \tag{5}$$

For a thermo-visco-elastic response of material, the deformation in the body is within the elastic limit, and the process can be considered reversible. For a reversible process, the temperature gradients in the body is infinitely small [27]. For a thermo-plastic material the process is irreversible, wherein the assumption of elastic recovery does not hold good. This gives

$$\gamma = 0,\ \theta_{,i} = 0 \Rightarrow \frac{\partial\psi}{\partial t} = -s\dot{\theta} + \frac{1}{\rho}\sigma_{ij}\dot{\varepsilon}_{ij}. \tag{6}$$

For a thermo-elastic material, the free energy ψ can be expressed by

$$\psi = \psi(\theta, \varepsilon_{ij}) \Rightarrow \frac{\partial\psi}{\partial t} = \frac{\partial\psi}{\partial\theta}\frac{\partial\theta}{\partial t} + \frac{\partial\psi}{\partial\varepsilon_{ij}}\frac{\partial\varepsilon_{ij}}{\partial t}. \tag{7}$$

By comparing eqns. (6) and (7), we get

$$s = \frac{-\partial\psi}{\partial\theta},\ \sigma_{ij} = \rho\frac{\partial\psi}{\varepsilon_{ij}}. \tag{8}$$

To obtain a generalized three-dimensional coupled thermo-mechanical model, consider an inelastic material

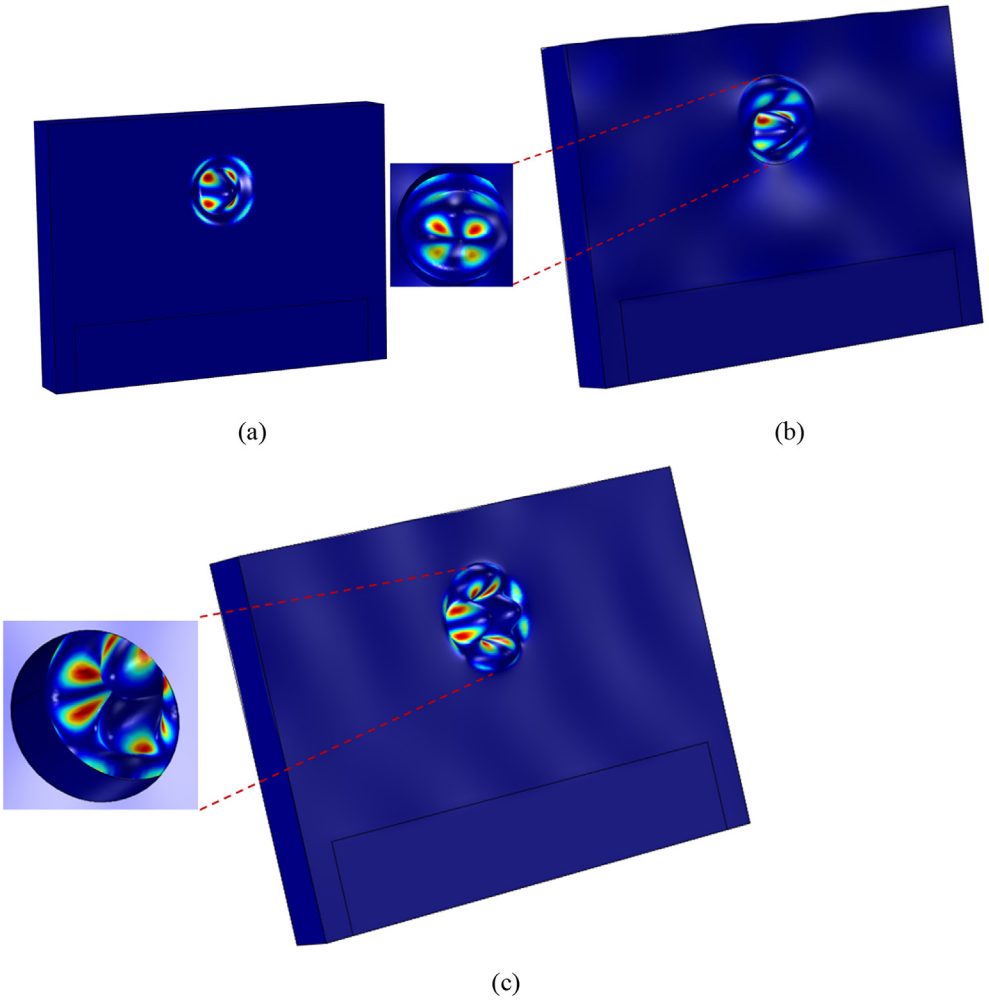

Fig. 7. Correlating shear strain mode shapes with the resonant mode shapes (see Fig. 6) for various different frequencies. (a) 30.15 kHz, (b) 45.041 kHz, and (c) 61.973 kHz.

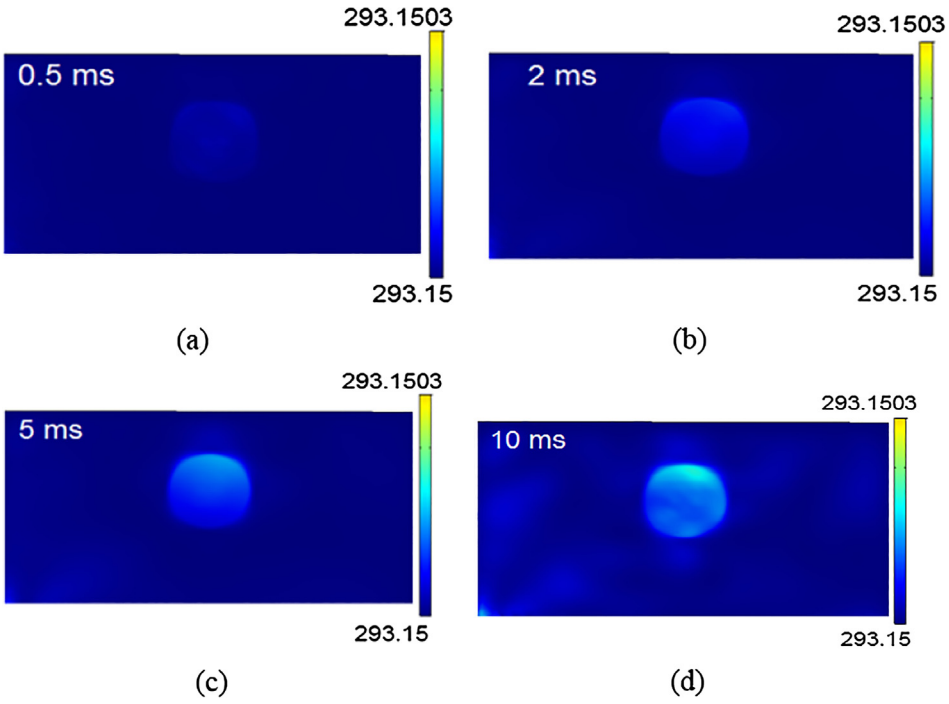

Fig. 8. Spatio-temporal temperature map obtained in the area of interest (see Fig. 3 (a)) at different time stamps. (a) 0.5 ms (b) 2 ms (c) 5 ms and (d) 10 ms.

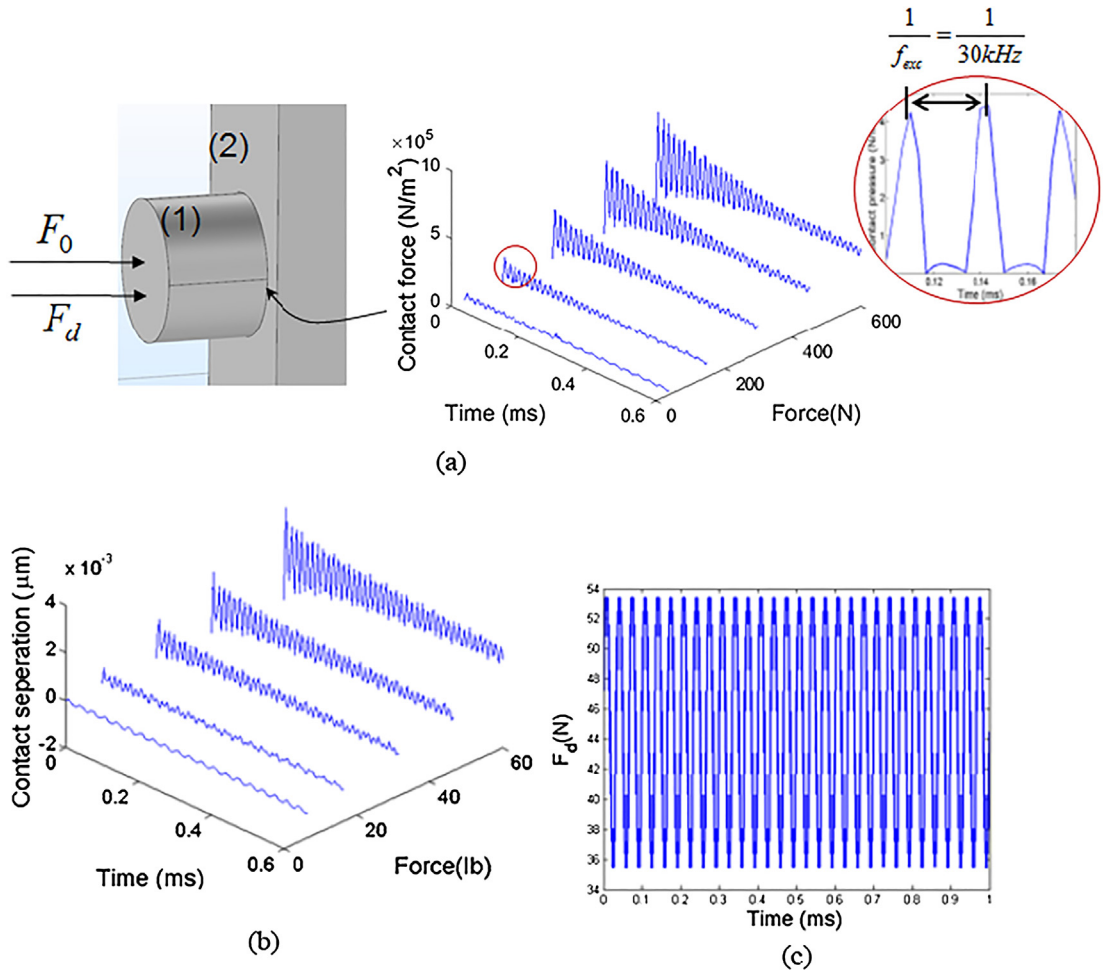

Fig. 9. (a) Dynamic contact force and (b) contact separation obtained at the contact interface for varying engagement force. (c) The dynamic excitation force (F_d) applied on the ultrasonic horn.

$$\psi = \psi(\theta, \varepsilon_{ij} - \varepsilon_{ij}^{ie}, k_a); \sigma_{ij} = \rho\frac{\partial\psi}{\partial\varepsilon_{ij}} + \sigma_{ij}^{v}, \tag{9}$$

where $\varepsilon_{ij} - \varepsilon_{ij}^{ie}$ is the state variable for inelastic behavior, and σ_{ij}^{v} denotes the viscous stress tensor. k_a is an additional set of internal variable or hidden variable, where $a = 1, 2, \ldots$, that characterize the inelastic material. We do not know the number and type of internal variables beforehand. They may be scalars or higher order tensors. However we represent these internal variables into the notation k_a. Further expressing $\frac{\delta Q}{dt}$ in terms of specific heat capacity at constant strain ($\varepsilon_{ij} = const$) gives

$$\frac{\delta Q}{dt} = \rho Cp\dot{\theta}. \tag{10}$$

Substituting Eqs. (9) and (10) in (1), and on further simplification gives

$$-\rho\theta\frac{\partial^2\psi}{\partial\theta^2}\dot{\theta} + \left(-\rho\theta\frac{\partial^2\psi}{\partial\varepsilon_{ij}\partial\theta} + \rho\frac{\partial\psi}{\partial\varepsilon_{ij}} - \sigma_{ij}\right)\dot{\varepsilon}_{ij} + \rho\left(\frac{\partial\psi}{\partial k_a} - \theta\frac{\partial^2\psi}{\partial k_a\partial\theta}\right)\dot{k}_a + \rho\left(\theta\frac{\partial^2\psi}{\partial\varepsilon_{ij}\partial\theta} - \frac{\partial\psi}{\partial\varepsilon_{ij}}\right)\dot{\varepsilon}_{ij}^{ie} = \rho Cp\dot{\theta} \tag{11}$$

For a constant strain, the viscous stress is zero, implies $\dot{\varepsilon}_{ij} = 0$. Neglect inelastic effects and internal variables for a thermo-elastic material. Further on substituting $\sigma_{ij} = \rho\frac{\partial\psi}{\varepsilon_{ij}}$ in Eq. (11) gives

$$-\theta\frac{\partial^2\psi}{\partial\theta^2} = Cp. \tag{12}$$

The constitutive equation relating the heat flux vector q_i and the temperature gradient $\theta_{,j}$ is a given by Fourier's heat conduction law,

$$q_i = -k_{ij}\theta_{,j}\ . \tag{13}$$

Substituting eqns. (4), (9), (11), (12) and (13) in (1) gives

$$\rho Cp\dot{\theta} = (K_{ij}\theta_{,j})_{,i} + r + \rho\theta\frac{\partial^2\psi}{\partial\varepsilon_{ij}\partial\theta}(\dot{\varepsilon}_{ij} - \dot{\varepsilon}_{ij}^{ie}) + (\sigma_{ij} - \sigma_{ij}^{v})\dot{\varepsilon}_{ij}^{ie} + \sigma_{ij}^{v}\dot{\varepsilon}_{ij}^{ie}. \tag{14}$$

For an isotropic material, the viscous stress is given by

$$\sigma_{ij}^{v} = \mu_{ij}\dot{\varepsilon}_{ij}, \tag{15}$$

where μ_{ij} is the coefficient of viscosity tensor. For thermo-elastic materials, expanding free energy $\psi(\theta, \varepsilon_{ij})$ using Taylor series at $\theta = \theta_0$ and imposing constant strain $\varepsilon_{ij} = 0$, gives

$$\psi(\theta, \varepsilon_{ij}) = \psi_0 + \left(\frac{\partial\psi}{\partial\varepsilon_{ij}}\right)_0\varepsilon_{ij} + \left(\frac{\partial\psi}{\partial\theta}\right)_0(\theta - \theta_0) + \frac{1}{2}\varepsilon_{ij}\left(\frac{\partial^2\psi}{\partial\varepsilon_{ij}\partial\varepsilon_{kl}}\right)_0\varepsilon_{kl} + \frac{1}{2}\left(\frac{\partial^2\psi}{\partial\theta^2}\right)_0(\theta - \theta_0)^2 + \left(\frac{\partial^2\psi}{\partial\varepsilon_{ij}\partial\theta}\right)_0(\theta - \theta_0)\varepsilon_{ij} \tag{16}$$

For zero stress in the reference state, the expression above reduces to

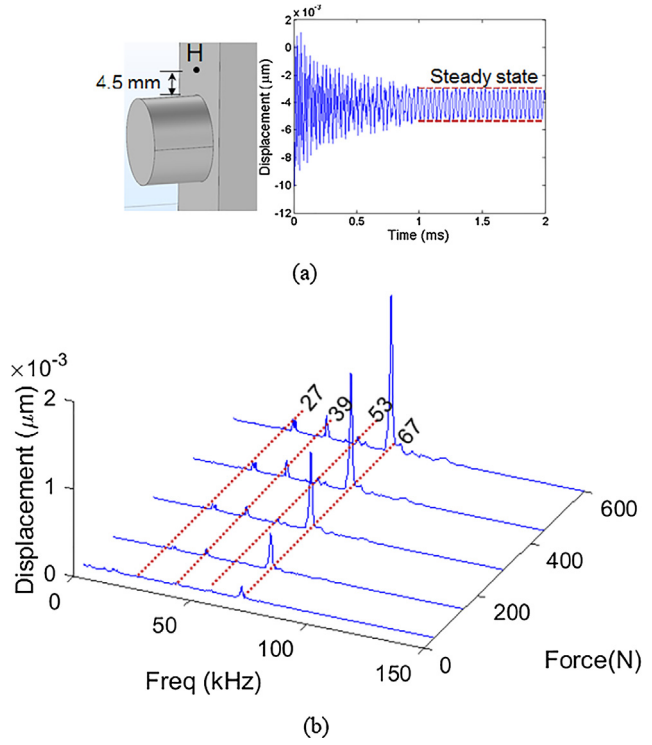

Fig. 10. Displacement-time history and frequency spectrum obtained at point 'H' after modeling contact mechanics are shown in (a) and (b) respectively.

$$\sigma_{ij} = D_{ijkl}(\varepsilon_{kl} - \varepsilon^0_{kl}); \quad D_{ijkl} = \rho\left(\frac{\partial^2\psi}{\partial\varepsilon_{ij}\partial\varepsilon_{kl}}\right); \quad \varepsilon^0_{kl} = \alpha_{ij}(\theta - \theta_0); \quad \alpha_{ij} = C_{ijkl}\beta_{kl}; \quad \beta_{ij} = -\rho\left(\frac{\partial^2\psi}{\partial\varepsilon_{ij}\partial\theta}\right)_0. \tag{17}$$

Substituting (15), (17) in (14) gives,

$$\rho C_p \frac{\partial T}{\partial t} = \nabla(k\nabla T) - 3K\alpha T(\dot{\varepsilon}_{ii}) + \mu_{ij}\dot{\varepsilon}_{ij}\dot{\varepsilon}_{ij}, \tag{18}$$

where K is the bulk modulus of elasticity, and α is the coefficient of thermal expansion. The terms $\nabla(k\nabla T)$, $3K\alpha T(\dot{\varepsilon}_{ii})$, $\mu_{ij}\dot{\varepsilon}_{ij}$ contribute to heat conduction, thermal expansion and heat generation in the material, respectively. On simplifying $\mu_{ij}\dot{\varepsilon}_{ij}\dot{\varepsilon}_{ij}$, using the symmetry property for coefficient of viscosity tensor and Cauchy strain tensor gives the coupled thermo-elastic equation for an isotropic material.

$$\rho C_p \frac{\partial T}{\partial t} = \nabla(k\nabla T) - 3K\alpha T(\dot{\varepsilon}_{ii}) + \mu_{\perp}(\dot{\varepsilon}_{11}\dot{\varepsilon}_{11} + \dot{\varepsilon}_{22}\dot{\varepsilon}_{22} + \dot{\varepsilon}_{33}\dot{\varepsilon}_{33}) + 2\mu_{||}(\dot{\varepsilon}_{12}\dot{\varepsilon}_{12} + \dot{\varepsilon}_{13}\dot{\varepsilon}_{13} + \dot{\varepsilon}_{23}\dot{\varepsilon}_{23}), \tag{19}$$

where $\mu_{\perp}$ and $\mu_{||}$ are the coefficients of viscosity associated with axial and shear strain terms respectively. The heat generation in the material due to axial and shear strain are given by $\mu_{\perp}(\dot{\varepsilon}^2_{11} + \dot{\varepsilon}^2_{22} + \dot{\varepsilon}^2_{33})$ and $\mu_{||}(\dot{\varepsilon}^2_{12} + \dot{\varepsilon}^2_{23} + \dot{\varepsilon}^2_{13})$, respectively. The developed model correlates each component of the strain rate with the generation of heat in the solid.

2.2. A model of dynamic contact between the horn and the target structure

In this section, the authors have developed a nonlinear dynamic contact model to capture the nonlinearities introduced due to horn

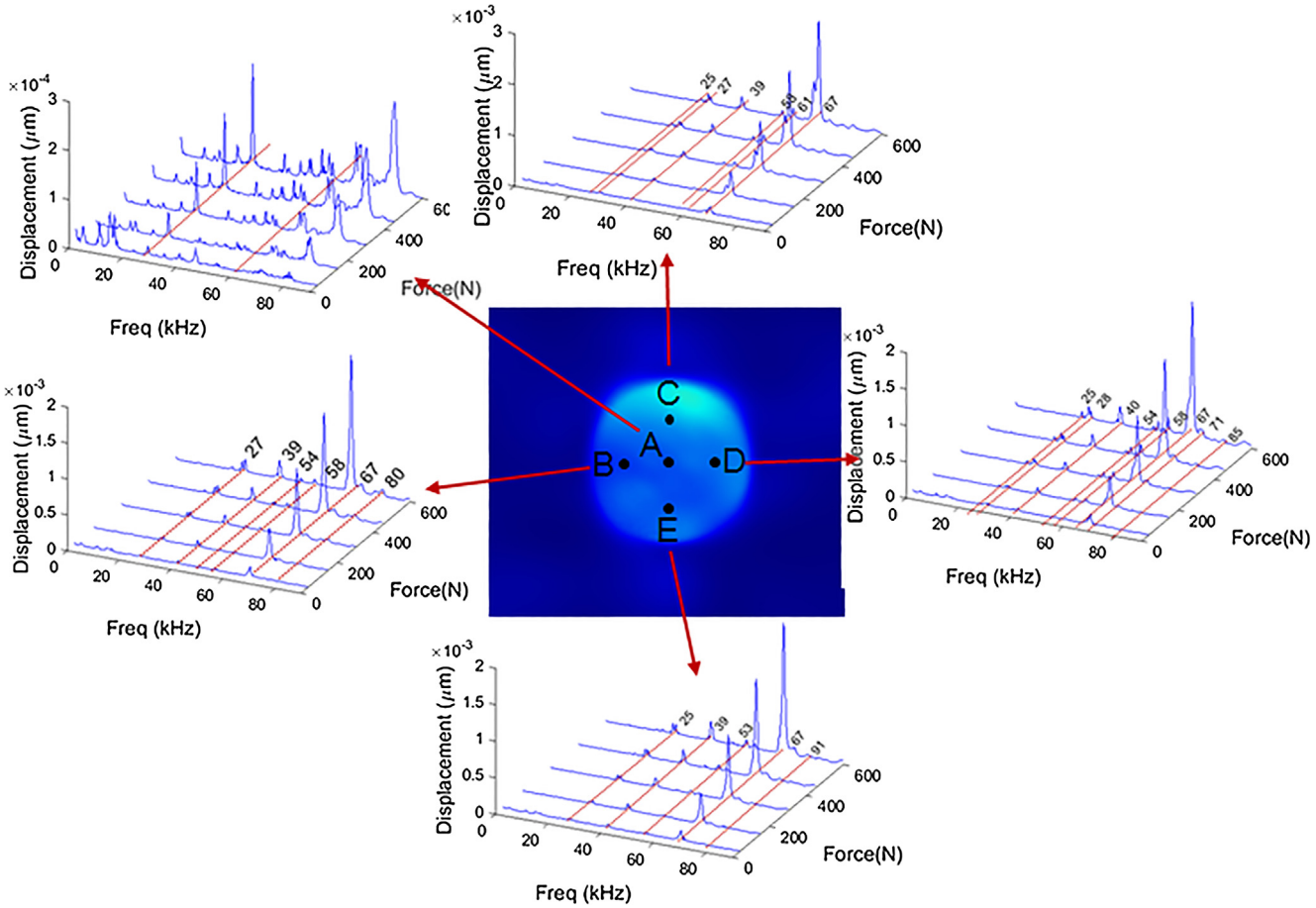

Fig. 11. Frequency spectrum showing various harmonics obtained at various locations in the SF. These simulation results are obtained after modeling contact mechanics between the horn and the target structure.

excitation, and contact interaction between the horn and the target structure (see Fig. 1). The model has been developed from the fundamentals of nonlinear dynamics. The developed model takes into account the effects of various sources of nonlinear vibration arising due to the amplitude of the excitation, engagement force on the target structure due to the ultrasonic horn, and the structural boundary conditions. The surface of the horn where engagement force is applied has been constrained in lateral directions to eliminate the rigid body motion of the horn (see Fig. 1(b)). The contact interface between the horn and the target specimen is modeled using a spring and a damper (see Fig. 1(b)). During the dynamic contact phenomena, the contact stiffness changes dynamically with respect to the compression and the expansion cycle of the horn. To capture this phenomenon a dynamic contact model is developed using a switching mechanism. The criteria for switching mechanism is given by *Case 1* and *Case 2*.

Case 1: When the displacement of the source (horn) surface ($u_x^{(1)}$) is less than the displacement of the destination (target structure) surface ($u_x^{(2)}$), a contact force (F_c) due to spring (k) and damper (C) is applied between both faces of the contact interface (source and destination surface).

$$u_x^{(1)} < u_x^{(2)} \Rightarrow F_c = k(u_x^{(2)} - u_x^{(1)}) + C(\dot{u}_x^{(2)} - \dot{u}_x^{(1)}). \tag{20}$$

Case 2: To eliminate impinging of the source (horn) on the destination (target structure), a multipoint displacement continuity constraint is applied at the contact interface.

$$u_x^{(1)} \geqslant u_x^{(2)} \Rightarrow u_x^{(1)} = u_x^{(2)}. \tag{21}$$

Instead of modeling the entire ultrasonic horn as a lumped mass, a segment of horn is modeled as a cylindrical mass (m_c), which gives high fidelity to the finite element based simulation scheme. The mass of the remaining segment of horn (m_H) is applied through a dynamic force (F_d) (see Fig. 1(c)), which is given by

$$F_d = (m_H - m_C)u_0\omega^2 \sin \omega t, \tag{22}$$

where u_0 is the amplitude of the excitation, ω is the excitation frequency in rad/s. The free body diagram at the contact interface for the horn and the target structure is shown in Fig. 1(c). The values of the parameters used in the model are given in Table 1. The developed model takes into account the effect of engagement force (F_0) on vibration and thermal characteristics. Future studies will be performed by introducing nonlinearities in the spring constant, which enables the model to be more accurate.

3. Optimization of heat generation from structural feature

Schematic showing the dimensions of the slab with pocket, various mechanical and thermal boundary conditions are shown in Fig. 2. At the location of vice both mechanically fixed ($u_x = u_y = u_z = 0$) and thermally insulated ($\dot{q} = 0$) boundary conditions are applied. Black body condition ($\xi = 1$) is applied to the surface that is viewed by thermal imager, and on all other surface, the emissivity of 6024 Aluminium alloy is applied ($\xi = 0.09$). ξ is the coefficient of emissivity. On all surface except the location of the vice region, the convective and radiative heat flux boundary conditions are applied.

$$\dot{q} = h(\theta - \theta_0) + \xi\sigma(\theta^4 - \theta_0^4), \tag{23}$$

where h is the convective heat transfer coefficient, σ is the Stefan-Boltzmann constant, θ_0 is the reference temperature. The convergence of the time domain simulation is ensured by satisfying the Courant-Friedrichs-Lewy (CFL) condition. The detailed procedure for calculating time steps and mesh size from the CFL criteria can be found in the reference [28].

The frequency of interrogation for vibro-thermography is optimally chosen using the knowledge obtained from fundamental of guided wave propagation (see reference [29,30] and references therein). From literature, it could be inferred that the amplitude of the out-of-plane material displacement is one order high, compared to its corresponding in-plane displacements. To obtain higher out-of-plane displacements, an asymmetric slot with respect to the neutral plane is designed. Maximum temperature rate in the SF is obtained when the dimensions of the SF are matched for resonance at the excitation frequency of horn. A perfect flexural resonance occurs in the SF, when the dimensions of SF matches with the asymmetric wavelength (λ). This concept is called resonance due to wavelength scale effect of SF.

The frequency of excitation is obtained from anti-symmetric guided wave dispersion curve (see Fig. 2(b)). In this paper, the diameter (λ) of slot is 34.7 mm. The dispersion curves are obtained for SF having 1 mm thickness. Using dispersion information, the optimal frequency of excitation for SF of diameter λ is estimated as 30 kHz. The target structure is excited at 30 k Hz with prescribed sinusoidal displacement (see Fig. 2). The displacement-time history and frequency spectrum obtained at point 'H' are shown in Fig. 3(a) and (b) respectively. To identify maximum heating rate, the sizes of the slot are varied for various multiples of wavelength (λ, $3\lambda/4$, $\lambda/2$) (see Fig. 4). Corresponding to each of these case, displacement, shear strain rate and temperature rate are calculated at point A. From the simulation results, the temperature rate is maximum for slot with diameter λ (see Fig. 4). For all further simulations, SF with diameter λ is chosen. The main contributing factor for temperature rise is due to $\mu_\perp(\dot{\varepsilon}_{11}^2 + \dot{\varepsilon}_{22}^2 + \dot{\varepsilon}_{33}^2)$ and $\mu_{||}(\dot{\varepsilon}_{12}^2 + \dot{\varepsilon}_{23}^2 + \dot{\varepsilon}_{13}^2)$. To characterize heat generation in the resonance vibration of SF, earlier reported studies use semi-empirical model, where the heat generation is entirely due to out-of-plane vibration, without accounting the effect of in-plane displacement components. The present model incorporates the effect of both in-plane and out-of-plane components and is thermodynamically consistent and is derived from the first and second law of thermodynamics.

To further validate the concept of resonance due to wavelength scale effect of SF, an Eigen value analysis is performed to obtain the natural frequencies and the mode shapes. Simulation are performed on a plate structure with SF having highest temperature rate (SF dia = λ). The displacement resonant modes and strain rate resonant modes obtained for various different frequencies are shown in Figs. 6 and 7, respectively. Although the structure is excited axially, the first flexural resonance of the SF is obtained at 30.15 kHz (see Fig. 6(a)). The heat generation rate in the SF is maximized, by optimally choosing the excitation frequency with reference to the first flexural resonant mode of the SF.

To validate the developed heat generation model, simulations are performed on a plate structure with SF having highest temperature rate (SF dia = λ) (see Fig. 4(d)). A spatio-temporal temperature distribution at different time stamps are analyzed in the area of interest (Fig. 4(a)). The spatio-temporal distribution gives a better insight about the propagation of the transient heat flux in the test structure and at the region of SF. The spatio-temporal thermal patterns at different time stamps are shown in Fig. 8. The ultrasonic horn excites the target structure at 30 kHz (f_{exc}). The images were obtained at the surface where emissivity $\xi = 1$. The images clearly indicate rise in temperature in the region of SF, where the excitation frequency for thermographic inspection is optimally chosen based on a relationship between the SF sizes with reference to wavelength based resonance phenomenon. Solodov et al. [14], characterized the resonant vibrations of SF using measurements with an infrared camera. The thermosonic patterns are interpreted with the help of hysteretic damping model that only accounts for in-plane polarization components of vibration.

4. The effect of engagement force on vibro-thermography

To study the effect of engagement force on vibro-thermography, simulations are performed on a plate with SF (see Fig. 1(a)). The contact dynamics of the ultrasonic horn with the target structure is simulated using the developed model in Section 2.2. In addition to engagement force (F_0), the ultrasonic horn is excited with the dynamic

force (F_d) (see Eq. (22), Fig. 9(c)). The dynamic force accounts for the segment of horn which is not elasto-dynamically modeled in the finite element simulation. Parametric study has been done by varying the engagement force from 0 to 600 N. Fig. 9(b) and (c) shows the dynamic contact force and the contact separation obtained at the contact interface for varying engagement force. From the simulations, it could be observed that, the magnitude of dynamic contact force and contact separation increases with engagement force. This is in accordance with the fundamentals of engineering mechanics. With increasing engagement force, the contact pressure at the interface increases. Thus gives higher rebound energy during the contact phenomenon. This essentially increases the contact separation distance between the horn and the target structure. By closely observing the frequency of contact, it confirms to be the frequency of excitation (f_{exc}) (see the inlet figure in Fig. 9(a)), which indeed validates the nonlinear dynamic contact model. During vibro-thermography the surface of ultrasonic horn is parallel to the surface of target structures. This ensures that energy from the horn is transmitted to the target specimen with minimum loss of energy. Misalignment of ultrasonic horn introduces non-uniform contact pressure, stress localization in the sub-surface region of contact. When the engagement force increases, the average kinetic energy increases, and tends to saturate when the engagement force exceeds certain value [20]. It is safe to say that an increase in the engagement force can improve the energy transfer efficient of the ultrasonic horn into the test plate. The frequency spectrum of vibration for a point close to excitation position 'H' for different engagement forces are shown in Fig. 10(b). The amplitude of excitation frequency, sub-super harmonics and super-harmonics increases with the excitation frequency, which demonstrate good agreement with the experiment observation in reference [20].

Without modeling dynamic contact between the horn and the target specimen, the response spectrum at the point 'H' is sharply tuned to excitation frequency (f_{exc}) (see Fig. 3(c)). On the other hand, by introducing contact mechanics model, higher harmonics are introduced in the response spectrum, even though the exciter is sharply tuned to its resonant frequency (see Fig. 10).

Dynamic response in the region of SF for without and with contact mechanics model are shown Figs. 5 and 11, respectively. Simulations results indicate that the engagement force significantly changes the dynamic behavior of the target structure (see Figs. 10(b) and 11). Higher engagement force generates higher nonlinear interaction giving rise to additional spectral components. Although the excitation using ultrasonic welder is sharply tuned to its resonant frequency, the effect of engagement force, and contact mechanics between horn and target structure introduces nonlinearities in the form of sub-super-harmonics, ultra-sub-harmonics, and chaos (see Fig. 11(c)). These nonlinear dynamics in the target structure are hypersensitive to amplitude of excitation, the location of the horn, the engagement force acting on the target structure due the horn, and structural boundary conditions.

5. Conclusion

In this paper, the phenomenon of vibro-thermography is modeled for ultrasonic horn excitation. The heat generation mechanism is modeled using a generalized three-dimensional coupled thermo-elastic model. The model correlates each component of the strain rate with the heat generation in the solid. Further, contact dynamics of ultrasonic actuator with the target structure is modeled, which captures various sources of nonlinear vibration. The sources of nonlinearity include amplitude of excitation, the effect of engagement force on the target structure due to the horn, and structural boundary conditions. Using the developed models a quantitative investigation has been done on a plate with a SF. A simulation scheme is developed which captures resonance due to wavelength scale effect of structural feature. The model can be used to aid in the optimization of the experimental measurements. This scheme establishes an optimal relation between the excitation frequency and the dimensions of the structural feature. Thus optimal choice of frequency of excitation during vibro-thermographic inspection enables to maximize the heat generation in the structural feature.

From the contact dynamic simulations, it has been observed that sub-harmonics, super-harmonics, sub-super harmonics and chaos are all present in the target structure even though the exciter is sharply tuned to its resonant frequency. It could be inferred that these nonlinear dynamics are hypersensitive to boundary conditions, location of excitation, and interaction between horn and target structure at the contact interface. An exact model of horn, target structure, boundary condition, and coupling materials are required to replicate the experimental behavior exactly. Furthermore, using the developed models, a spatio-temporal temperature distribution has been obtained in the target structure. This gives a better insight into propagation of transient heat flux in the test structure and at region of SF. The developed model can be further extended to understand the vibro-thermographic behavior in complex structural components with different kinds of hidden defects. The model can be further improvised by taking the effect of directional preference in the material properties. Anisotropy of constituent material phases influence the microstructure of material, which is true for both metal and composite. Naturally, these influences would appear in damping as well, which would affect the storage and loss modulus. The standard linear solid model of constituent phases may be used in a micro-mechanics framework to obtain such effects in a combined manner for storage and loss modulus as a function of frequency. This remain an important area and future scope of study for more accurate thermal signature in alloys and composites.

Acknowledgement

The authors thankfully acknowledge financial support from Pratt and Whitney USA under the grant number 24101 to carry out this research.

References

[1] L. Favro, et al., Infrared imaging of defects heated by a sonic pulse, Rev. Sci. Instrum. 71 (6) (2000) 2418–2421.
[2] S.D. Holland, et al., Quantifying the vibrothermographic effect, NDT and E Int. 44 (8) (2011) 775–782.
[3] L. Favro, et al., Sonic infrared imaging of fatigue cracks, Int. J. Fatigue 23 (2001) 471–476.
[4] R. Mignogna, et al., Thermographic investigation of high-power ultrasonic heating in materials, Ultrasonics 19 (4) (1981) 159–163.
[5] G. Busse, D. Wu, W. Karpen, Thermal wave imaging with phase sensitive modulated thermography, J. Appl. Phys. 71 (8) (1992) 3962–3965.
[6] T. Zweschper, A. Dillenz, G. Busse, Ultrasound lock-in thermography- a defect-selective NDT method for the inspection of aerospace components, Insight (2001).
[7] Han, X., et al., Recent developments in thermosonic crack detection. in AIP Conference Proceedings. 2002. AIP.
[8] C. Zhao-Jiang, et al., Finite element modeling of heating phenomena of cracks excited by high-intensity ultrasonic pulses, Chin. Phys. B 19 (11) (2010) 118104.
[9] D. Wu, et al., Nondestructive inspection of turbine blades with lock-in thermography, Materials Science Forum, Trans Tech Publ, 1996.
[10] T. Zweschper, et al., Ultrasound excited thermography using frequency modulated elastic waves, Insight-Non-Destruc. Test. Condi. Monit. 45 (3) (2003) 178–182.
[11] J. Rantala, D. Wu, G. Busse, Amplitude-modulated lock-in vibrothermography for NDE of polymers and composites, Res. Nondestr. Eval. 7 (4) (1996) 215–228.
[12] M. Genest et al. Comparison of thermography techniques for inspection of fiber metal laminates. 18th annual ASNT research symposium and spring conference. St. Louis, MO, USA. 2009.
[13] I. Solodov, J. Bai, G. Busse, Resonant ultrasound spectroscopy of defects: case study of flat-bottomed holes, J. Appl. Phys. 113 (22) (2013) 223512.
[14] I. Solodov, D. Derusova, M. Rahammer, Thermosonic Chladni figures for defect-selective imaging, Ultrasonics 60 (2015) 1–5.
[15] Szwedo, M., L. Pieczonka, T. Uhl., Application of vibrothermography in non-destructive testing of structures, in: 6th European Workshop on Structural Health Monitoring. 2012.
[16] W. Farren, G. Taylor, The heat developed during plastic extension of metals, Proceedings of the royal society of London A: mathematical, physical and engineering sciences, The Royal Society, 1925.
[17] J. Mason, A. Rosakis, G. Ravichandran, On the strain and strain rate dependence of the fraction of plastic work converted to heat: an experimental study using high speed infrared detectors and the Kolsky bar, Mech. Mater. 17 (2–3) (1994) 135–145.

[18] P. Rosakis, et al., A thermodynamic internal variable model for the partition of plastic work into heat and stored energy in metals, J. Mech. Phys. Solids 48 (3) (2000) 581–607.
[19] F. Mabrouki, et al., Numerical modeling of vibrothermography based on plastic deformation, NDT and E Int. 43 (6) (2010) 476–483.
[20] C.-S. Zhang, et al., Effect of engagement force on vibration characteristics and frictional heating in sonic IR imaging, NDT and E Int. 76 (2015) 52–60.
[21] F.-Z. Feng, et al., Effect of engagement force on vibration characteristics in sonic IR imaging, Ultrasonics 56 (2015) 473–476.
[22] X. Han, et al., Acoustic chaos for enhanced detectability of cracks by sonic infrared imaging, J. Appl. Phys. 95 (7) (2004) 3792–3797.
[23] X. Han, et al., Acoustic chaos and sonic infrared imaging, Appl. Phys. Lett. 81 (17) (2002) 3188–3190.
[24] I. Solodov, et al., Nonlinear self-modulation and subharmonic acoustic spectroscopyfor damage detection and location, Appl. Phys. Lett. 84 (26) (2004) 5386–5388.
[25] X. Han, et al., Mechanical model for the generation of acoustic chaos in sonic infrared imaging, Appl. Phys. Lett. 85 (8) (2004) 1332–1334.
[26] K. Zheng, et al., A dynamical model of subharmonic generation in ultrasonic infrared thermography, Ultrasonics 44 (2006) e1343–e1347.
[27] N.S. Ottosen, M. Ristinmaa, The Mechanics of Constitutive Modeling, Elsevier, 2005.
[28] B. Ghose, et al., Two dimensional FEM simulation of ultrasonic wave propagation in isotropic Solid Media using COMSOL, COMSOL Conference, (2010).
[29] G. Kolappan Geetha, et al., Laser Doppler imaging of delamination in a composite T-joint with remotely located ultrasonic actuators, Compos. Struct. 147 (2016) 197–210.
[30] P.D. Wilcox, Lamb Wave Inspection of Large Structures Using Permanently Attached Transducers, University of London, 1998.